Title

Reconciling the discrepancy between the dehydration rates in mantle olivine and pyroxene during xenolith emplacement

Authors

Xu, Yongjiang
Tang, Wenting
Hui, Hejiu
et al.

Publication Date

2019-12-01

DOI

10.1016/j.gca.2019.09.023

Peer reviewed

Available online at www.sciencedirect.com

ScienceDirect

Geochimica et Cosmochimica Acta 267 (2019) 179–195

Geochimica et Cosmochimica Acta

www.elsevier.com/locate/gca

Reconciling the discrepancy between the dehydration rates in mantle olivine and pyroxene during xenolith emplacement

Yongjiang Xu [a], Wenting Tang [a], Hejiu Hui [a,*], Roberta L. Rudnick [b,c], Sheng Shang [a], Zhongtian Zhang [a,1]

[a] State Key Laboratory for Mineral Deposits Research & Lunar and Planetary Science Institute, School of Earth Sciences and Engineering, Nanjing University, Nanjing 210023, China

[b] Department of Earth Science, University of California at Santa Barbara, Santa Barbara, CA 93106, USA

[c] Department of Geology, University of Maryland, College Park, MD 20742, USA

Received 22 January 2019; accepted in revised form 11 September 2019; Available online 19 September 2019

Abstract

Hydrogen concentration profiles through olivine and pyroxene in peridotite xenoliths carried in rift basalts from northern Tanzania (Lashaine, Eledoi, and Kisite localities) show bell-shaped distributions, indicating that diffusive hydrogen loss has occurred in all minerals. Homogeneous major element concentrations and equilibration of hydrogen between the cores of olivine and coexisting pyroxene suggest that hydrogen loss resulted from diffusive degassing during host magma emplacement. For these samples, hydrogen diffusivities in olivine and coexisting pyroxene must be within the same order of magnitude, similar to experimentally determined diffusivities, but in contrast to previous observations made on xenolithic peridotites. We demonstrate here, for the first time using natural samples, that significant differences in activation energy is likely the primary parameter that causes the discrepancy between hydrogen diffusion in olivine and pyroxene observed in different suites of mantle xenoliths. Because hydrogen diffuses faster in olivine than in pyroxene as temperature increases, hydrogen loss in the Tanzanian mantle xenoliths must have occurred at relatively low temperatures (~750 to ~900 °C), whereas hydrogen loss observed in previous xenolith studies likely occurred at higher temperatures (~950 to >1200 °C). Thus, the diffusive loss of hydrogen in the Tanzanian mantle xenoliths may have occurred at shallow depths or at the Earth's surface.

Keywords: Hydrogen; Diffusion; Mantle xenolith; Nominally anhydrous mineral; Tanzanian craton

1. INTRODUCTION

Nominally anhydrous minerals (NAMs), such as olivine and pyroxene incorporate trace amounts of "water" as hydrogen impurities in their crystal lattice defects bonded to structural oxygen (e.g., Bell and Rossman, 1992; Demouchy and Bolfan-Casanova, 2016). As olivine and pyroxene are the most abundant minerals in Earth's upper mantle, even the small amount of hydrogen they contain may significantly affect mantle physical properties, such as viscosity, electrical conductivity, and seismic wave attenuation (e.g., Karato and Jung, 1998; Mackwell et al., 1985; Wang et al., 2006). Consequently, much attention has been paid to the abundance and distribution of hydrogen in mantle olivine and pyroxene from xenolithic peridotites (e.g., Peslier et al., 2002, 2010, 2012, 2015; Demouchy et al., 2006; Grant et al., 2007; Li et al., 2008; Xia et al., 2010; Denis et al., 2013; Warren and Hauri, 2014; Hui et al., 2015; Satsukawa et al., 2017).

* Corresponding author.
E-mail address: hhui@nju.edu.cn (H. Hui).
[1] Current address: Department of Geology and Geophysics, Yale University, New Haven, CT 06511, USA.

https://doi.org/10.1016/j.gca.2019.09.023
0016-7037/

Previous studies of mantle xenoliths find that hydrogen in olivine is often partially lost through diffusive degassing, due to a decrease in water fugacity during xenolith emplacement (e.g., Demouchy et al., 2006; Li et al., 2008; Denis et al., 2013; Peslier et al., 2008, 2015). By contrast, hydrogen in coexisting pyroxene is generally homogeneously distributed, indicating no hydrogen was lost from pyroxene during emplacement. The only exceptions are orthopyroxenes in Tianchang xenoliths (Tian et al., 2017) and San Carlos veined peridotite xenoliths (Denis et al., 2018), which show hydrogen diffusion profiles in orthopyroxene that can be interpreted to be caused by melt-rock reaction (Tollan et al., 2015; Denis et al., 2018). However, hydrogen is homogeneously distributed in coexisting clinopyroxene in both cases, and no hydrogen has been detected in the coexisting olivine (i.e., dehydrated olivine, dehydrating orthopyroxene, and clinopyroxene not dehydrated; Denis et al., 2018). Thus, all previous investigations of mantle xenoliths infer that hydrogen diffusion in olivine is faster than that in pyroxene, yet laboratory experiments have shown that hydrogen diffusivities in olivine and pyroxene overlap (e.g., Farver, 2010; Demouchy and Bolfan-Casanova, 2016; Tian et al., 2017).

The discrepancy between hydrogen diffusivity inferred from measurements on xenoliths compared to experimental data could potentially undermine the conclusion that hydrogen contents of xenolithic pyroxene represent mantle concentrations (e.g., Peslier et al., 2012; Warren and Hauri, 2014; Hui et al., 2015). Various hypotheses have been proposed to explain the differences (Peslier, 2010), including the possible differences between laboratory setting and natural condition (e.g., Sundvall and Stalder, 2011; Denis et al., 2018), and different diffusion mechanisms of hydrogen in olivine and pyroxene (e.g., Demouchy et al., 2006; Grant et al., 2007; Ferriss et al., 2016). However, none of these hypotheses explain all the observations on natural samples, and this apparent paradox remains unsolved.

In this study, we determined hydrogen contents of coexisting olivine and pyroxene in peridotitic xenoliths from northern Tanzania using polarized Fourier transform infrared spectroscopy (FTIR). We observe hydrogen diffusion profiles in all minerals in these xenoliths, the first such discovery of hydrogen diffusion profiles preserved in coexisting olivine and pyroxene. These data help to reconcile experimental data versus results for natural samples, and suggest that differences in activation energy are the cause for previously inferred diffusivity differences between olivine and pyroxene in natural samples.

2. SAMPLES AND ANALYTICAL METHODS

The mantle xenoliths analyzed in this study are a suite of sixteen peridotite xenoliths collected from the Lashaine, Eledoi, and Kisite volcanoes, which form part of the eastern branch of the East Africa Rift that lies within the Mozambique Belt of northern Tanzania (Table 1). The xenoliths consist of harzburgite, lherzolite, and wehrlite (Table 1), displaying coarse-granular or coarse-tabular textures (Rudnick et al., 1994; Aulbach et al., 2011; Baptiste et al., 2015). Previous studies document the mineralogy, *P-T* equilibration conditions, Li isotope, and radiogenic isotopic compositions (Sm-Nd, Rb-Sr) of a subset of the Lashaine samples studied here (Rudnick et al., 1994; Aulbach and Rudnick, 2009; Aulbach et al., 2011). In addition, microstructures, crystal preferred orientations, and olivine hydrogen contents for some of the Lashaine and Eledoi samples were reported by Baptiste et al. (2015).

The samples are generally fresh and may contain hydrous minerals: phlogopites and pargasitic amphiboles (Rudnick et al., 1994; Baptiste et al., 2015), in addition to the nominally anhydrous minerals olivine, orthopyroxene, clinopyroxene, garnet and/or spinel (chromite) (Table 1). Olivine is typically inclusion-free, with grain size ranging from several hundred micrometers to several millimeters. Orthopyroxenes are usually smaller than olivines. Cracks are abundant in orthopyroxene from samples 89–664 and 89–674. Clinopyroxene, pale green and discretely distributed in the groundmass, often contains inclusions, including CO_2-rich fluid inclusions, and cracks, and may even shows symplectic textures (Rudnick et al., 1994).

Representative mineral grains of olivine, orthopyroxene, and clinopyroxene were hand-picked under a binocular microscope from gently-crushed whole rocks. Grains were selected to avoid fractures or inclusions and then were washed with ethanol and deionized water in an ultrasonic cleaner and then dried at room temperature overnight. The dried mineral grains were then embedded in epoxy resin and subsequently doubly polished using a Buehler grinder and an automatic polisher with diamond suspension (down to 1 μm). The polished mineral sections were cleaned with acetone, ethanol, and deionized water. The grain thicknesses, measured using a Mitutoyo digimatic micrometer, mostly ranged from 70 to 300 μm (EA1 and EA2). The polished sections were placed in a desiccator for at least 24 hours before analyses to eliminate potential surface water. The hydrogen and major-element contents of mineral grains were determined using an FTIR and an electron probe microanalyzer (EPMA), respectively.

2.1. Hydrogen analyses

The crystallographic orientation of each polished mineral grain was determined using interference figures under a petrographic microscope. Only grains having polished surfaces perpendicular to the principle axes (optic normal, acute bisectrix, or obtuse bisectrix) were used for FTIR analyses. Polarized infrared spectra of olivine and pyroxene with wavenumber from 650 to 7000 cm^{-1} were collected using a Continuμm microscope attached to a Nicolet iS50 FTIR spectrometer at Nanjing University. A liquid nitrogen-cooled mercury cadmium telluride (MCT) detector, a KBr beam splitter, and a 32× infrared objective were used during FTIR analyses. Aperture size from 30 × 30 to 80 × 80 $μm^2$ was chosen depending on the grain size, and the distribution of fractures and inclusions in the mineral grain. A wire-grid Zn-Se polarizer rotated parallel to the optical indicatrix α, β, or γ was used during FTIR analyses. Each analysis, consisting of 256 or 512 scans, was performed in a pre-dried N_2 gas environment to minimize interference from atmospheric water vapor. Systematic

Table 1
Summary of mantle xenoliths analyzed in this study.

Sample	Locality	Lithology[a]	Modal mineralogy[b] (%)	Equil. T (°C) [c]
89–661	Lashaine	Garnet Lherzolite	**Ol**$_{86.9}$**Opx**$_{6.1}$**Cpx**$_{4.2}$Grt$_{2.1}$Sp$_{0.5}$	1090
89–663	Lashaine	Harzburgite	**Ol**$_{82.8}$**Opx**$_{11.5}$Sp$_{1.4}$Phl$_{3.2}$	1300
89–664	Lashaine	Garnet Harzburgite	**Ol**$_{88.8}$**Opx**$_{9.7}$Cpx$_{0.8}$Grt$_{tr}$Sp$_{tr}$Phl$_{3.0}$	1250
89–669	Lashaine	Websterite	**Ol**$_{86.0}$Opx$_{0.9}$Cpx$_{8.6}$Sp$_{tr}$Phl$_{3.0}$	1000
89–672	Lashaine	Dunite	**Ol**$_{96.2}$Opx$_{tr}$**Cpx**$_{3.8}$	1080
89–674	Lashaine	Garnet Lherzolite	**Ol**$_{79.7}$**Opx**$_{11.4}$Cpx$_{5.8}$Grt$_{1.4}$Sp$_{0.5}$Phl$_{1.0}$	1240
89–675	Lashaine	Garnet Harzburgite	**Ol**$_{72.2}$**Opx**$_{24.0}$Cpx$_{1.8}$Grt$_{2.0}$Sp$_{0.5}$	1260
89–719	Lashaine	Garnet Harzburgite	**Ol**$_{82.9}$**Opx**$_{11.5}$Cpx$_{1.2}$Grt$_{4.5}$	1150
LS-4	Lashaine	Garnet Lherzolite	**Ol**$_{78.0}$**Opx**$_{14.0}$**Cpx**$_{3.0}$Grt$_{5.0,}$ Phl	1230
LS-8[d]	Lashaine	Harzburgite	**Ol**, Opx, **Cpx**, Phl	
LS-9	Lashaine	Lherzolite	**Ol**$_{73}$**Opx**$_{19.0}$**Cpx**$_{8.0}$	1060
LS-11	Lashaine	Garnet Harzburgite	**Ol**$_{82.0}$**Opx**$_{13.0}$**Cpx**$_{3.0}$Grt$_{2.0}$	1210
LS-15	Lashaine	Dunite	**Ol**$_{100.0}$	
EL-3	Eledoi	Harzburgite	**Ol**$_{88.0}$**Opx**$_{11.0}$**Cpx**$_{1.0,}$ Phl, Am	1100
EL-8	Eledoi	Harzburgite	**Ol**$_{92.0}$Opx$_{6.0}$**Cpx**$_{2.0}$	1090
KS-1[d]	Kisite	Lherzolite	**Ol**, Opx, **Cpx**, Sp	

Ol = olivine, Opx = orthopyroxene, Cpx = clinopyroxene, Grt = Garnet, Sp = spinel (chromite), Phl = phlogopite, Am = amphibole, and tr = trace amount.

[a] Lithology are from Rudnick et al. (1994), Baptiste et al. (2015), or this study (LS-8 and KS-1).

[b] Modal mineralogy are from Rudnick et al. (1994), Baptiste et al. (2015), or this study (LS-8 and KS-1). Minerals in bold are the ones analyzed using FTIR in this study.

[c] Equilibrium temperatures were calculated using the two-pyroxene geothermometer (Brey and Köhler, 1990). Major element compositions of mantle phases used to calculate temperature are from Rudnick et al. (1994) or Baptiste et al. (2015). Pressures used for samples 89–661 and 89–675 are from Rudnick et al. (1994). Pressures are assumed to be 3 GPa (slightly lower than the spinel-garnet transition pressure of Lashaine peridotites; Rudnick et al., 1994) for garnet-free samples 89–663, 89–669, 89–672, LS-9, EL-3, and EL-8.

[d] Modal mineralogy not determined.

cross-sectional analyses were then applied to the grains with heterogeneous distribution of O-H absorbance. Typically, at least one new background spectrum was collected every two hours.

Each spectrum was normalized to 1 cm thickness, and the baseline was manually corrected using the Omnic© software. The O-H absorbance for each principle direction (A_α, A_β, or A_γ) was determined by integrating the area beneath the O-H bands with the vector of the incident infrared light **E**//α, //β, or //γ. The modified Beer-Lambert equation was used to convert the total integrated absorbance ($A_{tot} = A_\alpha + A_\beta + A_\gamma$) to the hydrogen concentration (in ppm by weight of H_2O) in olivine and pyroxene:

$$C_{H_2O} = A_{tot}/I, \quad (1)$$

where I refers to the integral specific absorption coefficient of 5.32 ± 0.34 ppm^{-1} cm^{-2} (Bell et al., 2003) and 8.4 ± 0.42 ppm^{-1} cm^{-2} (Withers et al., 2012) for olivine, 15.6 ± 0.94 ppm^{-1} cm^{-2} for orthopyroxene (Bell et al., 1995), and 7.09 ± 0.32 ppm^{-1} cm^{-2} for clinopyroxene (Bell et al., 1995). At least two doubly polished grains were measured for each mineral in a xenolith to obtain A_{tot} (Table 2).

2.2. Major-element analyses

Major-element compositions of olivine, orthopyroxene, and clinopyroxene were measured using a JEOL JXA-8100M EPMA at Nanjing University or a JEOL JXA-8230 EPMA at China University of Geosciences (Wuhan) calibrated with natural and synthetic standards. Spot analyses were conducted using an accelerating voltage of 15 kV and a beam current of 20 nA. The electron beam size was 1 μm, with peak counting time varying from 10 to 25 s for different elements during each analysis. Cross-sectional measurements for representative olivine, orthopyroxene, and clinopyroxene grains in sample 89–661, and multi-spot analyses for the grains in some other samples were carried out to check for homogeneity of major-element distributions within the grain. Major-element X-ray maps (for Si, Ti, Al, Fe, Mg, Ca and Na) and backscattered electron (BSE) images were obtained for the selected olivine, orthopyroxene, and clinopyroxene grains using a Carl Zeiss Supra 55 field emission scanning electron microscope (SEM) at Nanjing University.

3. RESULTS

3.1. FTIR spectra

The polarized FTIR spectra of olivine and pyroxene obtained in this study (Fig. 1) have pleochroic O-H bands, similar to those of mantle xenoliths from other localities (e.g., Bell et al., 1995, 2003; Li et al., 2008; Sundvall and Skogby, 2011; Peslier et al., 2012; Hui et al., 2015). None of the spectra show C-H bands at 2700–3000 cm^{-1} (Fig. 1), indicating no interference from epoxy in the FTIR measurements. The polarized spectra of olivine with the electric vector parallel to (**E**//) γ have the strongest O-H absorbance (Fig. 1a and b). The orthopyroxene spectra obtained with **E**//γ also have the strongest absorbance, stretching from 2800 to 3700 cm^{-1} relative to those with **E**//α and **E**//β (Fig. 1c). The most prominent bands in the

Table 2
Polarized integrated O—H absorbances and hydrogen concentrations of olivine, orthopyroxene, and clinopyroxene in mantle xenoliths.

Sample	Olivine								Orthopyroxene				Clinopyroxene			
	A_α		A_β		A_γ		H_2O (ppm)[a]	H_2O (ppm)[b]	A_α	A_β	A_γ	H_2O (ppm)[c]	A_α	A_β	A_γ	H_2O (ppm)[c]
	Group I	Group II[e]	Group I	Group II[e]	Group I	Group II[e]										
Lashaine																
89–661	11.7		50.5		273.6		63 ± 9 (4)	40 ± 5	1200.0	667.7	2510.5	281 ± 37 (2)	702.2	767.9	471.8	274 ± 77 (3)
89–663	9.3		26.3		149.1		35 ± 5 (3)	22 ± 3	688.5[d]	1106.0	1721.3	225 ± 55 (2)				
89–664	3.9		34.6		264.7		57 ± 15 (4)	36 ± 9	81.1	122.5[d]	450.1	*41 ± 19* (3)				
89–669	6.2		21.2		241.7		51 ± 12 (4)	32 ± 7								
89–672	7.3		55.2		286.9		66 ± 16 (4)	42 ± 10					701.3	324.8	568.8	225 ± 33 (2)
89–674	5.1		16.9		257.7		53 ± 9 (3)	33 ± 5	452.1	346.7	1468.6	*145 ± 36* (2)				
89–675	8.6		29.4		159.4		37 ± 8 (4)	24 ± 4	819.7	520.5	2259.1	231 ± 46 (4)				
89–719	1.5		6.0		41.9		9.3 ± 2.7 (4)	5.9 ± 1.6	382.3	174.2	1004.0	100 ± 21 (3)				
LS-4	3.7	1.0	10.1	3.1	99.7		22 ± 3 (4)	14 ± 2	841.6	659.5	1988.0	224 ± 29 (2)	688.9	364.2	592.0	232 ± 49 (2)
LS-8	21.8		69.5		353.5		84 ± 13 (3)	53 ± 7					109.9	323.0	337.0	*109 ± 30* (2)
LS-9	9.6		25.9	11.5	159.8		38 ± 6 (5)	24 ± 3	1123.2	605.3	2388.9	264 ± 40 (5)	1063.6	1239.7	1094.3	479 ± 59 (3)
LS-11	5.9		25.1		107.7		26 ± 5 (3)	17 ± 3	953.5	744.7	2128.6	245 ± 33 (3)	622.1	932.5	828.6	336 ± 74 (4)
LS-15	1.8		16.9	6.4	107.7		24 ± 4 (3)	15 ± 2								
Eledoi																
EL-3	2.2	2.3	5.9	20.8	28.6	3.9	9.0 ± 1.8 (4)	5.7 ± 1.1	753.2	689.7	1573.8	193 ± 34 (4)	1155.5[d]	962.9	773.6	408 ± 62 (2)
EL-8	1.2		4.1	7.6	21.9	0.6	5.7 ± 2.0 (4)	3.6 ± 1.2					218.0	181.6	170.8	80 ± 12 (4)
Kisite																
KS-1				0.1	12.7		2.4 ± 0.7 (2)	1.5 ± 0.5					206.9[d]	172.3	220.9	*85 ± 23* (2)

[a] Numbers in parentheses indicate the number of grains analyzed for each type of mineral. The hydrogen concentrations in italic are the minimal estimations because no hydrogen plateaus were observed in the mineral grains. Olivine hydrogen concentrations were calculated with the integral specific absorption coefficients, 5.32 $ppm^{-1}\cdot cm^{-2}$ for Group I bands and 5.32×2.4 $ppm^{-1}\cdot cm^{-2}$ for Group II bands, respectively (Bell et al., 2003).

[b] Olivine hydrogen concentrations were calculated with the integral specific absorption coefficient of Withers et al. (2012).

[d] A_α or A_β was calculated based on the A_γ/A_α or A_γ/A_β from other samples because a grain with **E**// α or β was not present in the mineral mount.

[e] Group II bands in olivine were not considered in the diffusion modeling.

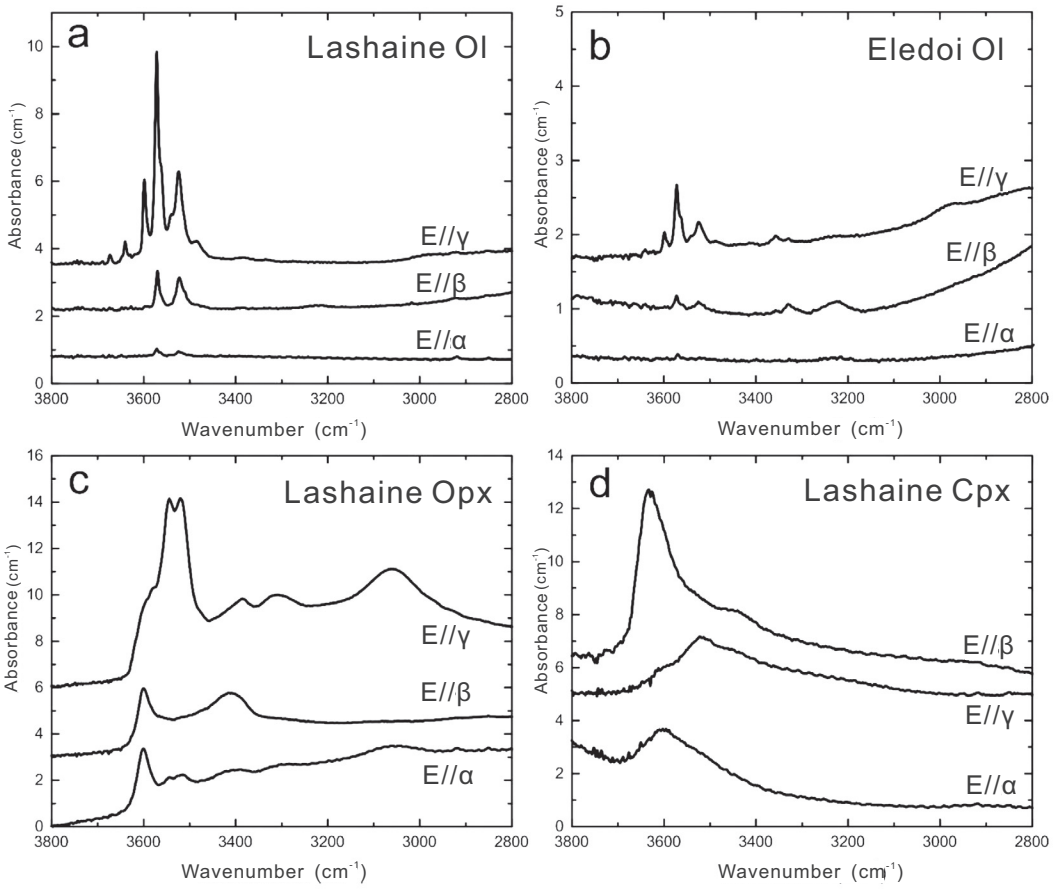

Fig. 1. Representative polarized FTIR absorption bands in the O-H vibration region of spectra for (a) Lashaine olivine (89–661), (b) Eledoi olivine (EL-3), (c) Lashaine orthopyroxene (89–661), and (d) Lashaine clinopyroxene (89–661). Spectra normalized to 1 cm thickness for three perpendicular directions (**E**//α, β and γ) are shifted vertically for comparison.

orthopyroxene spectra occur at 3510–3580 cm^{-1} on those with **E**//γ. The major O-H bands in the clinopyroxene spectra with **E**//α and **E**//β are both at ~3610 cm^{-1}, while those with **E**//γ occur at ~3510 cm^{-1} (Fig. 1d).

3.2. Hydrogen concentrations

Hydrogen is heterogeneously distributed in both olivine and pyroxene in all samples, as seen by the bell-shaped profiles (Fig. 2 and EA1). The lower O-H absorbance observed at the grain edges again indicates no interference from epoxy, which has much higher hydrogen concentration than any NAM. Despite the ubiquitous heterogeneous hydrogen distribution within each grain, 103 out of the 112 mineral grains analyzed, including both olivine and pyroxene, have preserved long homogeneous hydrogen concentration plateaus (Fig. 2 and EA1), which are representative of the initial concentration of hydrogen in these minerals (Thoraval and Demouchy, 2014). The other nine grains, which do not have hydrogen concentration plateaus, are either very small or have a lot of cracks. Therefore, the hydrogen concentrations of olivine and pyroxene in these mantle xenoliths can be calculated using the polarized O-H absorbances of the plateau at the grain centers (Table 2).

3.3. Major-element distributions

Major-element compositions of olivine and pyroxene in nine of sixteen xenoliths were measured in this study (Table 3). The olivine compositions in sample 89–661 obtained in this study (Table 3) are consistent with those determined previously (Rudnick et al., 1994). Cross-sectional analyses of olivine and pyroxene in sample 89–661 (Fig. 3), multi-spot analyses of mineral grains in some other samples (Table 3), as well as X-ray maps of major elements in minerals of samples 89–661 and 89–675 (Fig. 4), reveal homogeneous distributions of major elements in the olivine, orthopyroxene, and clinopyroxene grains analyzed in this study.

4. DISCUSSION

4.1. Inter-mineral equilibration of hydrogen

The linear correlation of Mg# [Mg/(Mg + Fe) × 100, using a.p.f.u (atom per formula unit) and all Fe as Fe^{2+}] between olivine and orthopyroxene in mantle xenoliths ($r^2 = 0.93$; Fig. 5a) suggests that the two phases are in equilibrium. However, the clinopyroxenes in Lashaine samples

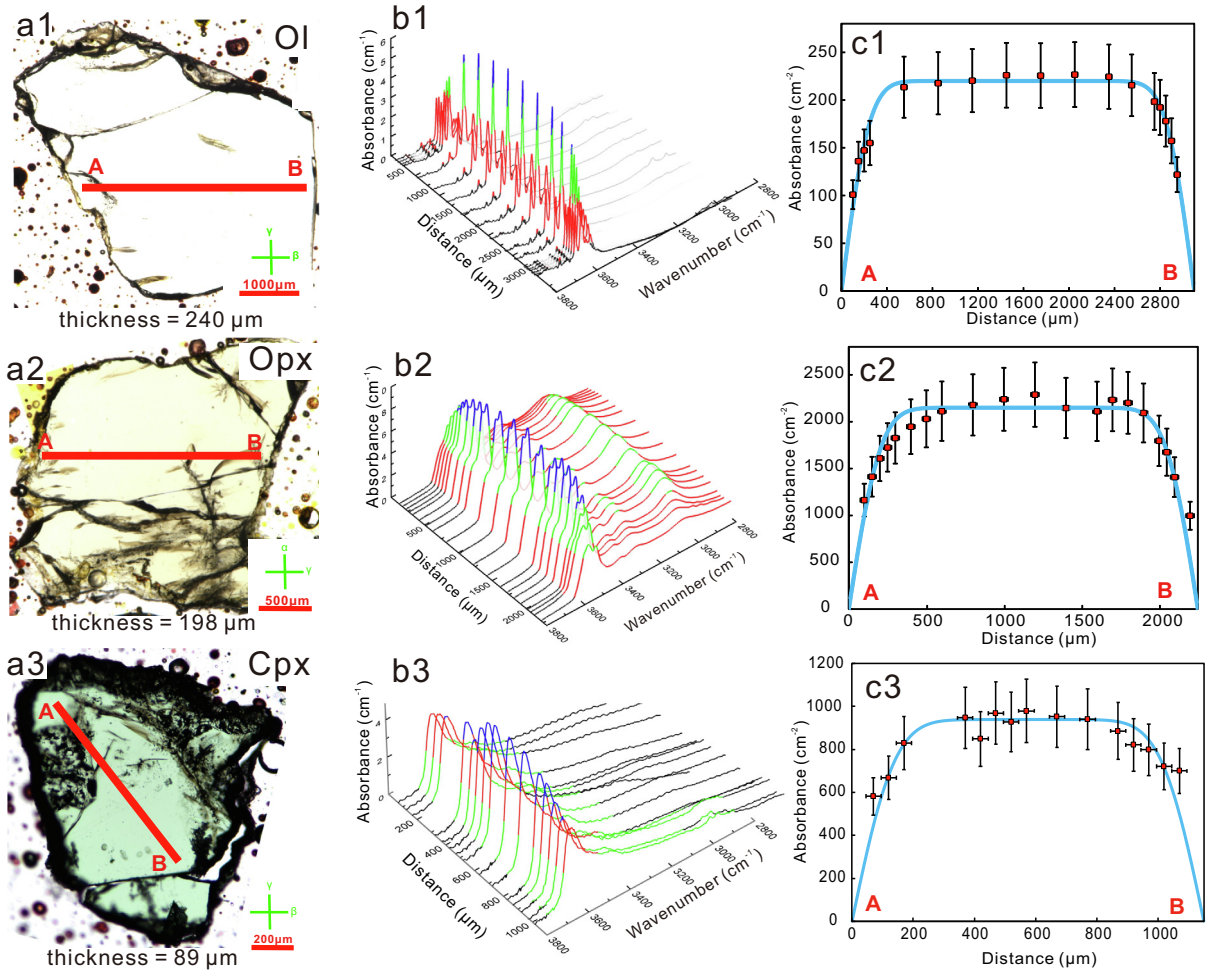

Fig. 2. O-H absorbance profiles in coexisting olivine and pyroxene of sample 89–661. (a) Plane-polarized light optical images showing the positions of FTIR analyses. (b) FTIR spectra with **E**//γ for olivine and orthopyroxene, and **E**//β for clinopyroxene, and (c) the integrated O-H absorbances with diffusion modeling results obtained along the profiles shown in (a).

89–664, 89–674, 89–675, LS-8, and LS-9, have Mg#s that lie off the equilibrium correlations for olivine ($r^2 = 0.93$) and orthopyroxene ($r^2 = 0.93$), respectively (Fig. 5b and c), and are unlikely to be in equilibrium with the coexisting olivine and orthopyroxene. The deviation from equilibrium indicates that these clinopyroxenes may be secondary or altered (Rudnick et al., 1994). Note, however, that the hydrogen partitioning between the coexisting phases could be in equilibrium, even if the major elements are not (Hui et al., 2015).

The ratios of hydrogen at the centers of coexisting olivine and pyroxene can be compared to the experimentally determined partition coefficients of hydrogen between these phases to assess whether hydrogen was in equilibrium in the minerals before the onset of hydrogen diffusive loss (Fig. 5d–f). However, experimental data reported in previous studies cover a wide range of pressures, temperatures, and compositions. This variability may reflect variable pressures and uncertainties associated with hydrogen analyses in olivine using secondary ion mass spectrometer (SIMS) (Demouchy et al., 2017). Therefore, the highest and lowest partition coefficients of hydrogen determined experimentally between coexisting phases at mantle condition from the literature (Hauri et al., 2006; Tenner et al., 2009; Kovàcs et al., 2012; Novella et al., 2014; Demouchy et al., 2017) have been used to assess the equilibration of hydrogen in the Tanzanian xenoliths.

Inter-phase equilibrium of hydrogen in Tanzanian samples seems to be largely preserved at the mineral centers, except for four samples: 89–664, 89–674, LS-8, and EL-3 (Fig. 5d and e). The orthopyroxenes in samples 89–664 and 89–674, and the clinopyroxene in sample LS-8 may have undergone extensive hydrogen loss, consistent with the lack of O-H absorbance plateaus in these minerals (EA1), and consistent with their deviation from equilibrium. It is not clear what may have caused the hydrogen concentrations of sample EL-3 to deviate from the equilibrium region for olivine and pyroxene (Fig. 5d and e), though we note that the hydrogen ratios between olivine and pyroxene in this sample are within the ranges observed in natural samples (Demouchy and Bolfan-Casanova, 2016). Furthermore, hydrogen in the cores of orthopyrox-

Table 3
Major-element compositions of olivine, orthopyroxene and clinopyroxene in mantle xenoliths.

Sample	89-661[b]			LS-4[c]			LS-8[c]		LS-9[c]			LS-11			LS-15[c]	EL-3			EL-8		KS-1	
	Ol	Opx	Cpx	Ol	Opx	Cpx	Ol	Cpx	Ol	Opx	Cpx	Ol	Opx	Cpx	Ol	Ol	Opx	Cpx	Ol	Cpx	Ol	Cpx
n.[a]	1(20)	1(20)	1(15)	3(3)	2(3)	2(2)	3(1–3)	4(1)	3(3)	3(3)	3(1)	1(3)	1(3)	2(–3)	4(2)	3(2–3)	1(2)	1(2)	2(2)	1(3)	2(3)	2(2)
SiO_2	41.49	57.42	54.93	41.26	57.40	54.05	41.26	54.98	41.42	56.54	54.40	41.34	57.90	55.14	40.22	41.62	56.97	53.73	41.77	54.93	40.56	53.60
TiO_2	–	0.09	0.29	–	–	–	–	0.28	–	–	0.12	–	–	0.10	–	–	0.06	0.52	–	–	–	0.23
Al_2O_3	–	1.51	3.70	–	0.91	2.24	–	1.56	–	1.39	3.23	–	0.89	2.82	–	–	2.05	3.92	–	1.61	–	2.39
Cr_2O_3	–	0.57	3.09	–	0.34	1.67	–	2.41	–	0.38	2.11	–	0.39	1.86	–	–	0.55	1.88	–	3.82	–	2.50
FeO	6.70	4.22	1.92	7.53	4.55	2.24	9.51	1.68	7.69	4.34	1.70	7.36	4.40	2.39	11.25	7.52	4.76	2.44	6.99	2.29	9.64	3.00
MnO	0.09	0.11	0.06	0.10	0.12	0.08	0.12	0.08	0.11	0.11	0.07	0.09	0.13	0.08	0.49	0.12	0.16	0.11	0.10	0.07	0.16	0.11
MgO	51.71	35.83	15.54	50.48	35.07	16.59	49.22	16.51	50.25	35.79	16.18	51.03	35.30	16.83	47.15	50.66	33.81	16.44	50.91	16.39	48.65	16.70
CaO	–	0.37	18.03	–	0.57	19.65	–	20.67	–	0.38	20.55	–	0.46	18.83	–	0.05	0.71	19.02	–	18.62	0.07	19.20
Na_2O	–	0.16	2.37	–	0.07	1.82	–	1.73	–	0.09	2.11	–	0.10	1.89	–	–	0.11	1.52	–	2.00	–	1.32
NiO	0.38	0.13	0.08	0.41	0.11	0.05	0.39	–	0.40	0.09	–	0.36	0.16	0.06	0.35	0.33	0.09	–	0.34	0.07	0.28	–
Total	100.37	100.41	100.01	99.78	99.14	98.39	100.50	99.90	99.87	99.11	100.47	100.18	99.73	100.00	99.46	100.30	99.27	99.56	100.11	99.80	99.36	99.05
Mg#	93.22	93.80	93.52	92.28	93.22	92.96	90.22	94.60	92.09	93.63	94.43	92.51	93.46	92.63	88.19	92.31	92.68	92.33	92.85	92.73	90.00	90.84

[a] n. is the number of grains analyzed for each type of mineral. Numbers in parentheses indicate the number of spots analyzed on each grain.
[b] The cross-sectional measurements were carried out on sample 89–661.
[c] Samples LS-4, LS-8, LS-9, and LS-15 were analyzed at Nanjing University, and the others were analyzed at China University of Geosciences (Wuhan).

ene and clinopyroxene of sample EL-3 is in equilibrium (Fig. 5f).

4.2. Hydrogen diffusion in Tanzanian olivine and pyroxene

Hydrogen in olivine and coexisting pyroxenes is heterogeneously distributed within the grains (Fig. 2 and EA1), in contrast to the major elements, which are homogenous. Thus, the distributions of hydrogen and major elements are not correlated, and it is unlikely that the bell-shaped profiles of O-H absorbance in olivine and pyroxene resulted from melt-rock interaction (Tollan et al., 2015), or new growth around pre-existing grains in a relatively dry magma (Denis et al., 2013), as these processes are expected to result in major element zoning. Rather, it is more likely that the heterogeneous distributions of hydrogen in coexisting olivine and pyroxene grains observed in this study resulted from diffusive loss of hydrogen during xenolith emplacement (e.g., Demouchy et al., 2006; Peslier et al., 2015). This is consistent with the decreases observed in hydrogen concentrations near cracks and fractures within several mineral grains (EA1). The profiles of integrated absorbance are similar to those of site-specific absorbance in olivine (EA3) and pyroxene (EA4), respectively. This similarity suggests that the hydrogen species in each mineral of this study have similar diffusivities. Therefore, we used the integrated absorbance of each mineral, to represent hydrogen concentration in diffusion profiles in this study, the same as previous studies (e.g., Xia et al., 2000; Demouchy et al., 2006; Peslier et al., 2008; Denis et al., 2013; Peslier et al., 2015; Tian et al., 2017).

The bell-shaped hydrogen concentration profiles can be fit by one-dimensional (1-D) or three-dimensional (3-D) diffusion modeling. Both laboratory experiments and numerical simulations have demonstrated that the hydrogen distribution in a mineral is typically controlled by hydrogen diffusion along its fastest axis (e.g., Thoraval and Demouchy, 2014; Ferriss et al., 2015; Demouchy et al., 2016), and, thus, 1-D modeling can be a good approximation (Thoraval and Demouchy, 2014). Furthermore, 1-D hydrogen diffusion modeling has been commonly used for both xenoliths and laboratory hydrogen diffusion experiments (e.g., Ingrin et al., 1995; Xia et al., 2000; Demouchy and Mackwell, 2003, 2006; Stalder and Skogby, 2003; Peslier et al., 2008; Jollands et al., 2016). Finally, we do not observe a large difference between hydrogen diffusion profiles along different axes for a given mineral grain (EA1). Therefore, 1-D diffusion modeling is used in this study to compare with previous results.

Assuming that the hydrogen concentration at the grain edge is 0, 1-D modeling was performed in Excel with the following equation (Shewmon, 1989):

$$c(x,t) = \frac{4c_o}{\pi}\sum_{j=0}^{\infty}\frac{1}{(2j+1)}\sin\frac{(2j+1)\pi x}{h}\hat{\mathrm{A}} \cdot \exp\left(-\left[\frac{(2j+1)\pi}{h}\right]^2 Dt\right), \quad (2)$$

where c is the hydrogen content expressed as the integrated O-H absorbance along a specific axis normalized to 1 cm

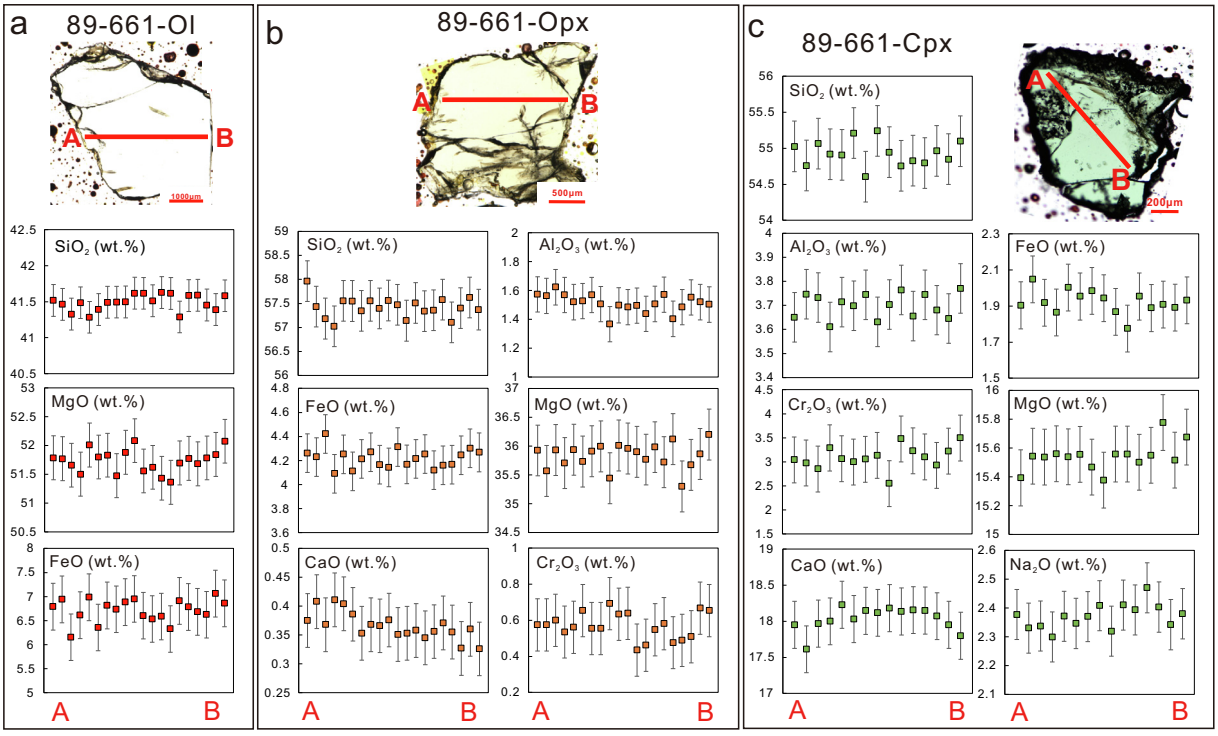

Fig. 3. Cross-sectional measurements of major elements in (a) olivine, (b) orthopyroxene, and (c) clinopyroxene of sample 89–661. The red lines in plane-polarized light optical images of the grains show the positions of analyses. Error bars represent the 2σ uncertainty. (For interpretation of the references to color in this figure legend, the reader is referred to the web version of this article.)

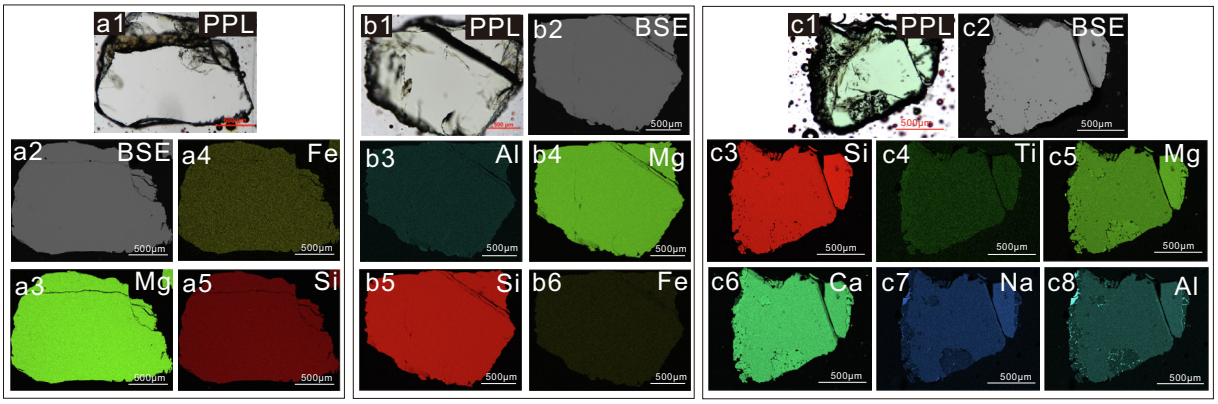

Fig. 4. Plane-polarized light optical images (PPL), back-scattered electron images (BSE) and X-ray maps of major elements in (a1–a5) olivine of sample 89–675, (b1–b6) orthopyroxene of sample 89–675, and (c1–c8) clinopyroxene of sample 89–661. Major elements are homogeneously distributed within each grain.

sample thickness, c_o is the initial O-H absorbance, x is the distance from the grain edge in m, h is the grain length from edge to edge in m, D is the diffusivity in m^2s^{-1}, t is the diffusion time in s, and j represents the index of summation. The first 100 terms (to obtain a smooth fitting curve) on the right side of Eq. (2) were used in the modeling. Following previous studies (e.g., Demouchy and Mackwell, 2003; Peslier et al., 2015), the diffusivity was assumed to be constant in each model. Therefore, the hydrogen diffusivity ratio between coexisting olivine and pyroxene (D_H^{Ol}/D_H^{Px}) can be obtained without knowing the exact diffusion temperature. Because the hydrogen diffusion times in both minerals are the same, this diffusivity ratio can be determined when the best fits are obtained simultaneously for diffusion profiles in both olivine and coexisting pyroxene for each sample. Note that different boundary conditions (i.e., whether the hydrogen concentration at the edge is 0) do not change the calculated hydrogen diffusivity ratio. The orthopyroxenes in samples 89–664 and 89–674 may have undergone loss of hydrogen through the abundant cracks

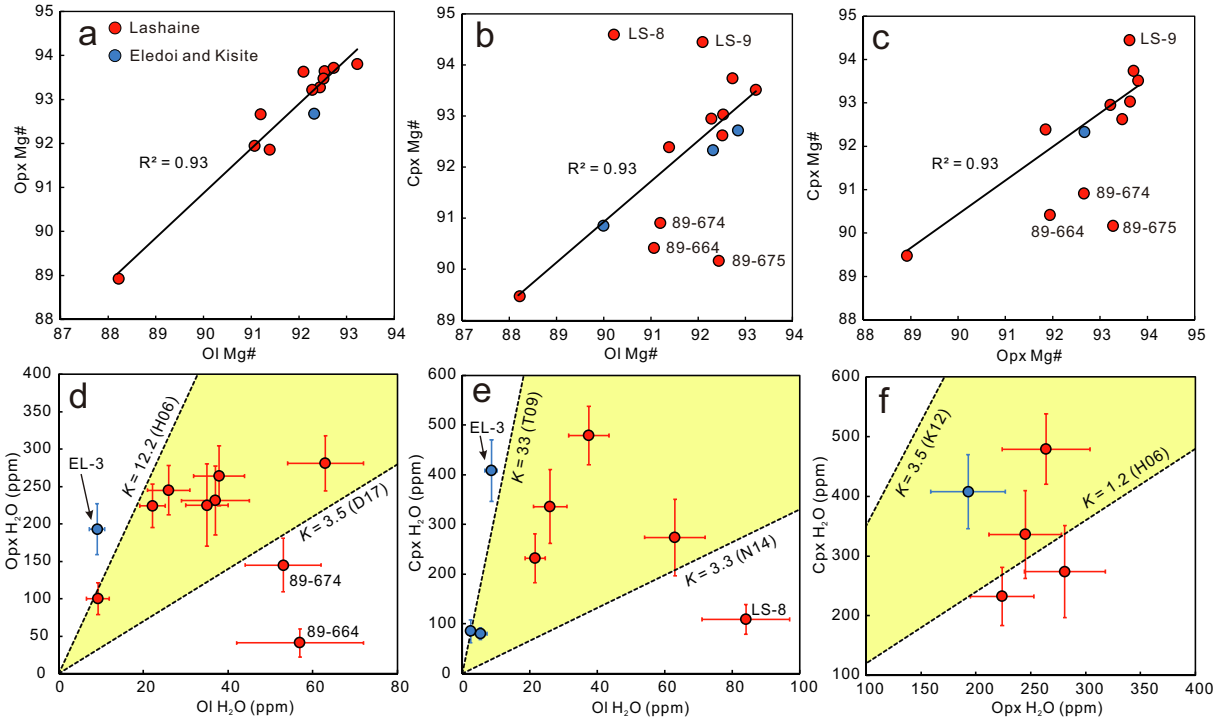

Fig. 5. Comparison of Mg# (a) between olivine and orthopyroxene, (b) between olivine and clinopyroxene, and (c) between orthopyroxene and clinopyroxene in mantle peridotitic xenoliths. The clinopyroxenes of samples 89–664, 89–674, 89–675, LS-8, and LS-9 lie off the correlation between olivine and orthopyroxene, suggesting multiple generations of clinopyroxene in these samples (Rudnick et al., 1994). Comparison of hydrogen distributions (d) between olivine and orthopyroxene, (e) between olivine and clinopyroxene, and (f) between orthopyroxene and clinopyroxene. The dashed lines correspond to different partition coefficients (K) of hydrogen (d) between orthopyroxene and olivine, (e) between clinopyroxene and olivine, and (f) between clinopyroxene and orthopyroxene from different experimental studies. The hydrogen concentrations of orthopyroxene in samples 89–664 and 89–674 and clinopyroxene in sample LS-8, which do not have the hydrogen plateaus at their grain centers, were calculated using the highest absorbances obtained. D17 = Demouchy et al. (2017), H06 = Hauri et al. (2006), K12 = Kovàcs et al. (2012), N14 = Novella et al. (2014), and T09 = Tenner et al. (2009).

within the grains. The hydrogen diffusion paths in these grains can be complicated and, thus, their data have not been used in diffusion modeling (EA1).

4.3. Comparison of D_H^{Ol}/D_H^{Px} in mantle xenoliths

The differences in observed hydrogen diffusion distances in olivine and coexisting pyroxene depends on the relative diffusivities of the two phases. Diffusion modeling of our results for the Tanzanian xenoliths suggest that hydrogen diffusivities in coexisting olivine and pyroxene are very similar: D_H^{Ol}/D_H^{Opx} vary from 1.4 to 2.6, and D_H^{Ol}/D_H^{Cpx} range from 1.0 to 3.5 (Table 4). These values fall within the range determined from laboratory diffusion experiments (e.g., Ingrin and Blanchard, 2006; Farver, 2010).

In contrast to our results, all previous studies made on xenolithic peridotites inferred that hydrogen diffuses much faster in olivine than coexisting pyroxene ($D_H^{Ol} \gg D_H^{Px}$). The hydrogen diffusivity in Tianchang xenolithic olivine is inferred to be at least 10 times larger than that in pyroxene ($D_H^{Ol}/D_H^{Px} \geq 10$; Tian et al., 2017). The shortest hydrogen diffusion distance in mantle olivine so far reported is about 200 μm, while there is no difference between inferred hydrogen contents at the center of an orthopyroxene grain and at a position 80 μm away from the grain edge (Doucet et al., 2014). Therefore, a conservative estimate of the hydrogen diffusivity ratio between olivine- and pyroxene-based diffusion modeling (Eq. (2)) from these earlier studies is $D_H^{Ol}/D_H^{Px} \geq 6$.

In summary, all previous studies of hydrogen distributions in xenolithic olivine and coexisting pyroxene have shown that $D_H^{Ol} \gg D_H^{Px}$. However, the hydrogen diffusion profiles recorded in olivine and pyroxene of the Lashaine, Eledoi, and Kistie mantle xenoliths show that there is no large difference between their diffusivities ($D_H^{Ol} \approx D_H^{Px}$).

4.4. Factors influencing hydrogen diffusion in olivine and pyroxene

It has been suggested that temperature, pressure, mineral chemical composition, and oxygen fugacity may all affect hydrogen diffusivities of mantle olivine and pyroxene (e.g., Ingrin et al., 1995; Hercule and Ingrin, 1999; Demouchy and Mackwell, 2003, 2006; Stalder and Skogby, 2003, 2007; Demouchy et al., 2016). By comparing our data with those of previous studies we explore the different parameters that influence hydrogen diffusion in the minerals of mantle xenoliths, aiming to understand the dis-

Table 4
Estimated diffusion temperature, duration, and diffusivity ratios of hydrogen between coexisting olivine and pyroxene in each mantle xenolith.

Sample	89–661	89–663	89–672	89–675	89–719	LS-4	LS-8	LS-9	LS-11	EL-3	EL-8	KS-1
T (°C)	860 ± 20	760 ± 10	880 ± 20	900 ± 10	750 ± 10	850 ± 20	*820 ± 20*	830 ± 10	770 ± 10	790 ± 20	800 ± 20	*810 ± 20*
t (h)	6 ± 1	20 ± 4	4 ± 1	2 ± 0.5	50 ± 10	6 ± 1	*6 ± 1*	5 ± 1	18 ± 4	8 ± 1	6 ± 1	*12 ± 3*
D_H^{Ol}/D_H^{Opx}	2.2 ± 0.8	1.5 ± 0.7		2.6 ± 0.6	1.4 ± 0.7	2.1 ± 0.9		2.0 ± 0.6	1.5 ± 0.8	1.7 ± 0.7		
D_H^{Ol}/D_H^{Cpx}	2.9 ± 1.0		3.5 ± 1.1			2.6 ± 1.2	*1.8 ± 1.0*	2.0 ± 0.6	1.0 ± 0.5	1.3 ± 0.9	1.4 ± 1.0	*1.6 ± 1.0*

Note: Numbers in *italic* are the lowest estimations because no hydrogen plateaus were observed in clinopyroxenes of these xenoliths.

crepancy between the results of laboratory experiments and the observations of previous mantle xenoliths studies.

4.4.1. Mineral chemistry

Laboratory experiments have demonstrated that mineral chemical composition can affect hydrogen diffusion in both olivine and pyroxene (e.g., Mackwell and Kohlstedt, 1990; Kohlstedt and Mackwell, 1998; Hercule and Ingrin, 1999). Iron may enhance hydrogen diffusion in olivine and pyroxene through Fe redox reaction (e.g., Skogby and Rossman, 1989; Mackwell and Kohlstedt, 1990). However, this effect is not significant enough to control hydrogen diffusion in natural olivine and pyroxene (Demouchy and Mackwell, 2006; Stalder and Skogby, 2007; Sundvall et al., 2009a). Furthermore, lattice defects related to different trivalent cations that can influence hydrogen incorporation, may play a more important role in influencing hydrogen diffusivity in natural pyroxenes (e.g., Stalder and Skogby, 2007; Sundvall et al., 2009a, 2009b). Aluminum and Cr, which may charge-couple with hydrogen to substitute for Si and Mg, respectively, may inhibit hydrogen diffusion in pyroxene (Stalder and Behrens, 2006; Ferriss et al., 2016). Indeed, a negative correlation has been observed between tetrahedral Al and hydrogen diffusivity in natural clinopyroxene (Ferriss et al., 2016). It has been further suggested that hydrogen diffusivity in orthopyroxene is correlated with its atomic ratios of Cr/Fe and Fe/(Cr + Al) (Stalder and Behrens, 2006). However, mineral compositions in the mantle xenoliths studied here are similar to those from previous studies in which hydrogen is inferred to diffuse much faster in xenolithic olivine than coexisting pyroxene (Fig. 6). This similarity suggests that mineral chemical composition is not a crucial parameter in explaining the different hydrogen diffusivity results. In other words, chemical compositions could have affected hydrogen diffusion in mantle minerals, but it did not cause the differences in hydrogen diffusion observed between this and previous studies.

4.4.2. Oxygen fugacity

Experimental data suggest that oxygen fugacity has little effect on hydrogen diffusivity in olivine (Mackwell and Kohlstedt, 1990; Jollands et al., 2016). Similarly, hydrogen diffusivity in clinopyroxene is independent of oxygen fugacity (Hercule and Ingrin, 1999). More importantly, the oxygen fugacities of our samples (Rudnick et al., 1994) fall within the range of those from previous studies (Fig. 7). Therefore, it is reasonable to infer that differences in oxygen fugacity are not responsible for the different hydrogen diffusivities inferred for olivine and pyroxene between this and previous studies.

4.4.3. Pressure

No pressure effect has been observed in hydrogen diffusion experiments in olivine conducted at pressures from 0.2 to 3 GPa (Kohlstedt and Mackwell, 1998; Demouchy and Mackwell, 2006; Demouchy et al., 2016). Furthermore, no difference has been observed between hydrogen diffusion experiments for orthopyroxene at pressures ranging from 1 bar to 1 GPa either (Carpenter, 2003). Similarly, diffusion

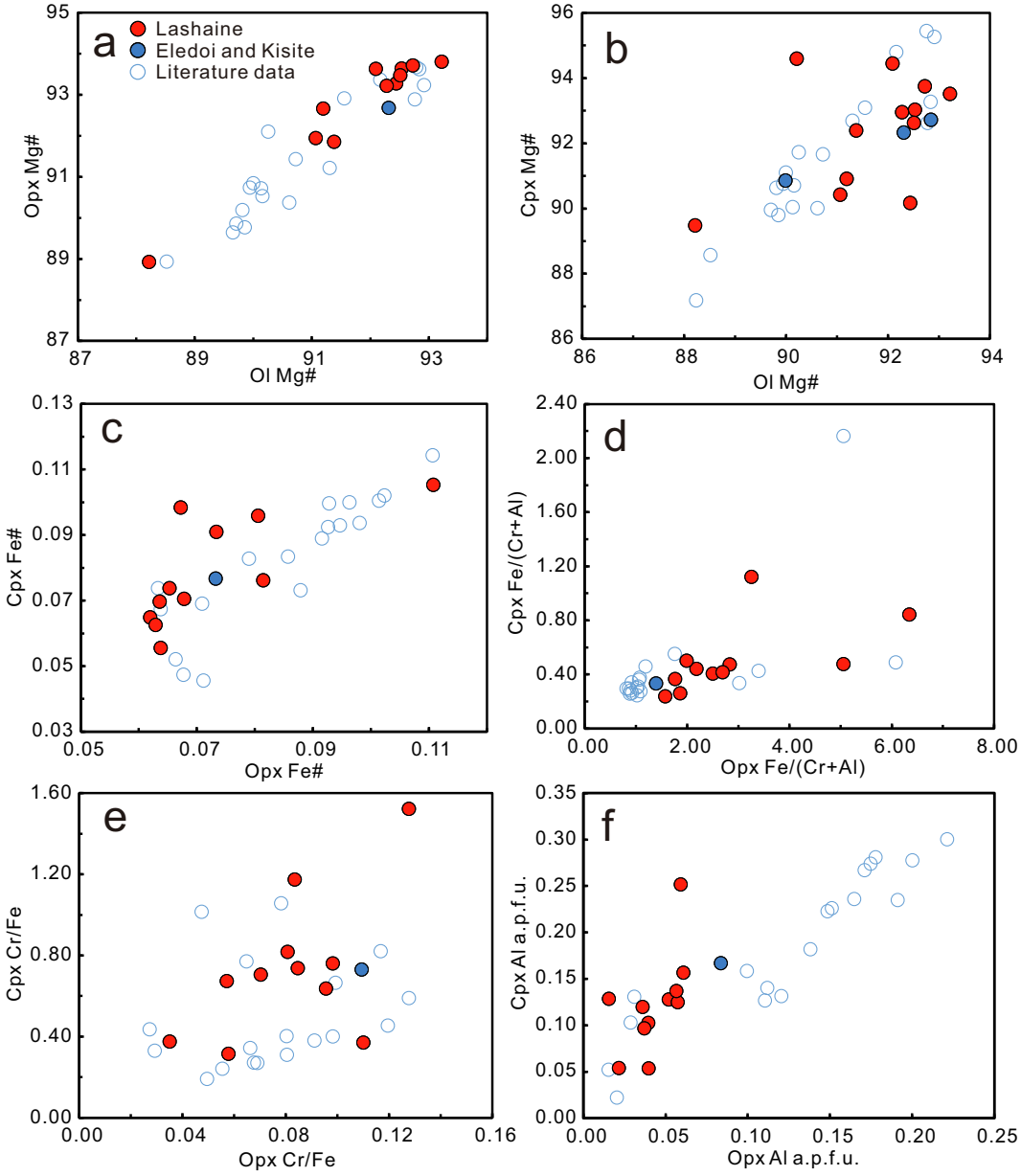

Fig. 6. Comparison of mineral major elements or element ratios between different mantle xenoliths. The solid circles represent samples in this study and the open circles are for those from previous studies (Luhr and Aranda-Gómez, 1997; Demouchy et al., 2006; Peslier and Luhr, 2006; Peslier et al., 2008; Denis et al., 2013; Doucet et al., 2014; Bizimis and Peslier, 2015). No obvious difference on chemical composition has been observed between xenoliths of this study and those in literature. Fe# is defined as Fe/(Mg + Fe) in mole fraction.

experiments for hydrogen in clinopyroxene carried out at pressures of up to 0.3 GPa (the highest pressure so far) suggest no pressure effect on hydrogen diffusivity in clinopyroxene (Weis et al., 2016). Therefore, the limited experimental data indicate that pressure variation within the lithosphere does not affect hydrogen diffusion in mantle minerals.

4.4.4. Temperature

Numerous studies have been carried out over a range of temperatures on hydrogen diffusion in olivine (Mackwell and Kohlstedt, 1990; Kohlstedt and Mackwell, 1998; Hauri, 2002; Demouchy and Mackwell, 2003, 2006; Demouchy, 2004; Chen et al., 2011; Gaetani et al., 2012; Lloyd et al., 2013; Padrón-Navarta et al., 2014; Demouchy et al., 2016; Jollands et al., 2016), orthopyroxene (Carpenter, 2003; Stalder and Skogby, 2003, 2007; Stalder and Behrens, 2006; Stalder et al., 2007; Sundvall and Skogby, 2011), and clinopyroxene (Ingrin et al., 1995; Dyar et al., 1996; Guilhaumou et al., 1998; Hercule and Ingrin, 1999; Woods et al., 2000; Xia et al., 2000; Ingrin and Blanchard, 2006; Sundvall et al., 2009a, 2009b; Sundvall and Skogby, 2011; Ferriss et al., 2016; Lloyd et al., 2016; Weis et al., 2016). However, data from different

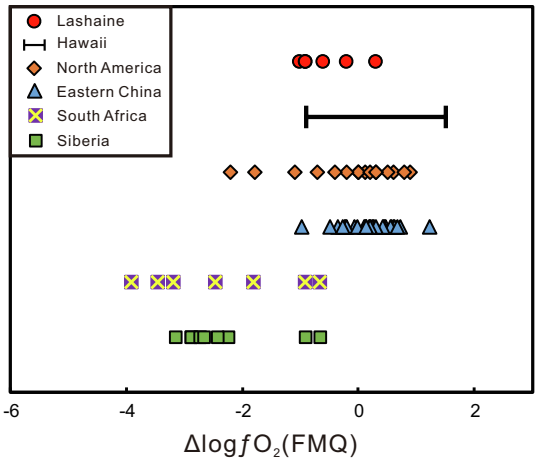

Fig. 7. Comparison of oxygen fugacities between different mantle xenoliths. No obvious difference on oxygen fugacity has been observed between mantle xenoliths in this study (Rudnick et al., 1994) and those from Hawaii (Peslier et al., 2015), North America (Peslier and Luhr, 2006), Eastern China (Yu et al., 2011), South Africa (Peslier et al., 2012), and Siberia (Doucet et al., 2014).

experimental studies are not always consistent with each other. In particular, the effects of temperature on hydrogen diffusivity is inconsistent from one study to the next (Farver, 2010; Demouchy and Bolfan-Casanova, 2016). Therefore, it is necessary to evaluate all available experimental data on hydrogen diffusivity and construct consistent relationships between hydrogen diffusivity and temperature for olivine, orthopyroxene, and clinopyroxene. Furthermore, two different mechanisms, proton-polaron (PP) and proton-vacancy (PV) processes, have been identified for hydrogen diffusion in olivine (Kohlstedt and Mackwell, 1998; Demouchy, 2010). Both mechanisms could have contributed to hydrogen diffusion in natural olivines and most laboratory diffusion experiments (Ferriss et al., 2018). It is difficult to assess the contribution of each mechanism to hydrogen diffusion in natural olivines. Therefore, we used all diffusivities reported from laboratory experiments to assess the temperature dependence of hydrogen diffusivity.

The following criteria have been used to assess the published experimental data. First, only diffusivity data obtained from hydrogen extraction or incorporation experiments were used; the data from isotope exchange experiments were not considered here because the diffusion mechanism in isotope exchange experiments is different from that in the hydration or dehydration process (Karato, 2013). Second, for consistency, the diffusivities obtained from hydrogen diffusion along the fastest axis were used, as both laboratory experiments and numerical simulations have shown that hydrogen distribution is controlled by diffusion along the fastest axis of the crystal (Thoraval and Demouchy, 2014; Ferriss et al., 2015; Demouchy et al., 2016). Third, the diffusivity data for hydrogen in synthetic pyroxene were excluded because hydrogen diffusion in pyroxene probably is sensitive to chemical compositions (e.g., Denis et al., 2018), and such synthetic pyroxenes are significantly compositionally different from natural pyroxenes (e.g., Stalder et al., 2005, 2007; Denis et al., 2018). Fourth, the hydrogen diffusivity data obtained from Jaipur diopside (Dyar et al., 1996; Woods et al., 2000; Ferriss et al., 2016) were also excluded because the samples have abundant inclusions (Ferriss et al., 2016) and cracks (Woods et al., 2000), and the diffusivities are very different from those of all other natural clinopyroxenes (Ferriss et al., 2016). Finally, only the diffusion experiments on which temperatures were measured directly, not assumed or calculated, were used for assessment of the temperature dependence of diffusivity.

Without knowing the exact mechanisms that controlled hydrogen diffusion in natural olivines, linear least squares regressions of all the evaluated experimental data were performed to establish the correlations between hydrogen diffusivity and temperature for olivine (Fig. 8a). The same procedure was also applied to orthopyroxene and clinopyroxene (Fig. 8b and c). In studies where no errors are reported for temperature, uncertainties were assigned as follows: we used ±2 °C for the vertical furnace experiments of Kohlstedt and Mackwell (1998) using the estimation of Stalder and Skogby (2003), ±25 °C for the piston cylinder experiments of Carpenter (2003) using the estimation of Bromiley et al. (2004), and ±10 °C for the TZM cold vessel experiments of Demouchy and Mackwell (2006) using the error estimation of Demouchy (2004). In studies where no error was reported for log$D$, uncertainties were assigned to be ±0.1 using the estimations of Stalder and Skogby (2003) and Stalder et al. (2007). Using the assessed experimental data, the temperature dependence of hydrogen diffusivity in olivine, orthopyroxene, and clinopyroxene is quantified as:

$$D_{\mathrm{H}}^{\mathrm{Ol}} = 10^{-(3.36\pm1.50)}\exp\left[-(187\pm35)\times\frac{1000}{RT}\right], \quad (3)$$

$$D_{\mathrm{H}}^{\mathrm{Opx}} = 10^{-(5.55\pm0.34)}\exp\left[-(147\pm8)\times\frac{1000}{RT}\right], \quad (4)$$

$$D_{\mathrm{H}}^{\mathrm{Cpx}} = 10^{-(9.21\pm0.88)}\exp\left[-(70\pm18)\times\frac{1000}{RT}\right], \quad (5)$$

where R is the gas constant, and T is the temperature in K.

The above equations suggest that the activation energy for hydrogen diffusivity in olivine is the highest, while that for clinopyroxene is the lowest. This means that the diffusivity of hydrogen in olivine increases much faster with increasing temperature than those for pyroxene (Fig. 8d). Therefore, differences in the temperature at which diffusion occurred may explain the differences inferred for hydrogen diffusivity from previous studies of mantle xenoliths and our results (Fig. 9). At high temperatures, a large amount of hydrogen may diffuse out of olivine, but there would be no noticeable hydrogen diffusion in coexisting pyroxenes. This may explain why previous studies of mantle xenoliths found hydrogen diffusive loss profiles only in olivine, and not in coexisting pyroxene. The diffusivity models (Fig. 8) suggest that at 1250 °C, hydrogen would diffuse more than 200 μm in olivine, but less than 74 μm in orthopyroxene, and about 8 μm in clinopyroxene, consistent with previous observations (e.g., Doucet et al., 2014). Consequently, it is difficult to document hydrogen diffusion

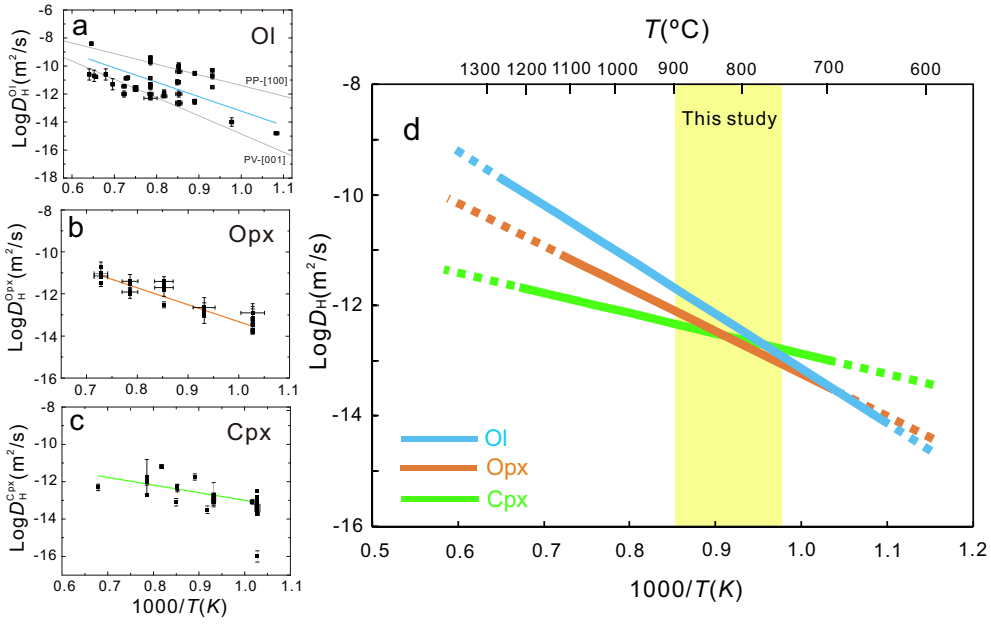

Fig. 8. Temperature dependence of hydrogen diffusivity in olivine and pyroxene based on experimental studies, as described in the text. Linear regressions with errors between hydrogen diffusivity and temperature of (a) olivine, (b) orthopyroxene, and (c) clinopyroxene, and (d) comparison of hydrogen diffusivity between olivine, orthopyroxene, and clinopyroxene. References: olivine (Mackwell and Kohlstedt, 1990; Kohlstedt and Mackwell, 1998; Hauri, 2002; Demouchy and Mackwell, 2003, 2006; Chen et al., 2011; Gaetani et al., 2012; Demouchy et al., 2016; Jollands et al., 2016; Ferriss et al., 2018), orthopyroxene (Carpenter, 2003; Stalder and Skogby, 2003; Sundvall and Skogby, 2011), and clinopyroxene (Ingrin et al., 1995; Guilhaumou et al., 1998; Hercule and Ingrin, 1999; Xia et al., 2000; Ingrin and Blanchard, 2006; Sundvall and Skogby, 2011; Ferriss et al., 2016; Weis et al., 2016). The two different hydrogen diffusion mechanisms identified in olivine: proton-polaron (PP) process along fast [100] axis (Kohlstedt and Mackwell, 1998; Demouchy, 2010) and proton-vacancy (PV) process along fast [001] axis (Demouchy and Mackwell, 2006; Demouchy, 2010) are also plotted respectively for comparison.

in pyroxene using FTIR if it has occurred at high temperature. In our study, the hydrogen diffusivity in olivine is similar to that in coexisting pyroxene ($D_H^{Ol}/D_H^{Opx} = 1.4–2.6$, $D_H^{Ol}/D_H^{Cpx} = 1.0–3.5$; Table 4), implying that the main stage of hydrogen diffusion in the Tanzanian samples likely occurred at relatively low temperatures of ~750 to ~900 °C (Figs. 8d and 9). The activation energy for hydrogen diffusion in Tanzanian olivines is intermediate between PP and PV rates (Fig. 8a; Kohlstedt and Mackwell, 1990; Demouchy et al., 2006; Demouchy, 2010). This is consistent with the observation that the hydrogen loss rates in natural olivines are controlled by both PP and PV processes (Ferriss et al., 2018).

4.5. Geological implications

The temperature of the host magma at the time of xenolith entrainment for the Tanzanian xenoliths was likely to have been quite high (>1100 °C; Burgi et al., 2002), based on the high MgO contents of the host lavas (Dawson et al., 1970). This is consistent with the relatively high equilibration temperatures for our samples calculated using the two-pyroxene geothermometer (Brey and Köhler, 1990), which vary from 1000 to 1300 °C (Table 1; Rudnick et al., 1994). However, our data suggest that hydrogen diffusion occurred at much lower temperatures, because if diffusion had occurred at the equilibrium temperatures, the hydrogen diffusion distance in olivine would be much longer than those in coexisting pyroxene.

The nature of host magmas, in particular, its volatile content, may influence when hydrogen diffusive loss occurs during xenolith entrainment and emplacement. The Lashaine lava, rich in alkaline and volatile contents (including 0.83 wt.% water), resembles ankaramite (Dawson et al., 1970). Likewise, a volcanological study of Eledoi finds that the host magma also contained very high volatile contents (Berghuijs et al., 2012). Hydrous mantle minerals, such as phlogopite and pargasitic amphibole, are commonly present in Lashaine (Rudnick et al., 1994; Baptiste et al., 2015) and Eledoi (Dawson and Smith, 1988) xenolithic peridotites (Table 1). All of these lines of evidence suggest that the host magma may have been hydrous initially. The hydrous host magma could have suppressed degassing of mantle xenoliths at an early stage. Therefore, the main stage of diffusive loss of hydrogen in the Tanzanian olivine and coexisting pyroxene may have been at shallow depths, or even on the surface.

Our results suggest that hydrogen diffusive loss in the coexisting olivine and pyroxene likely occurred mainly at temperatures of ~750 to ~900 °C (Eqs. (3)–(5), Table 4). The duration of hydrogen diffusion in olivine and coexisting pyroxenes is estimated to be between 2 and 50 h (Table 4). The eruptive phases at Lashaine that carried the xenoliths are carbonatite tuffs and ankaramitic scoria

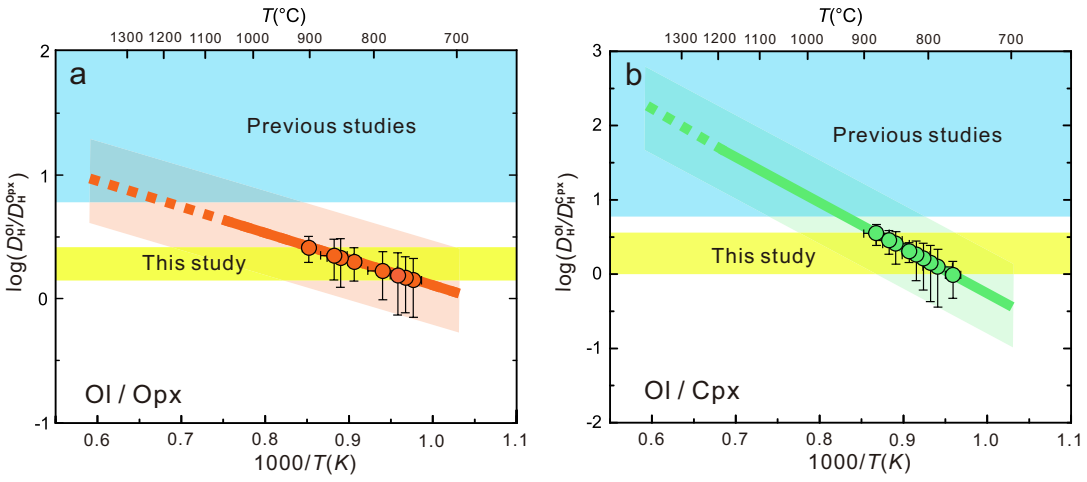

Fig. 9. Temperature versus hydrogen diffusivity ratio between olivine and pyroxene, (a) D_H^{Ol}/D_H^{Opx} at 700–1093 °C and (b) D_H^{Ol}/D_H^{Cpx} at 700–1200 °C. The dotted lines show extrapolations of the solid ones (Eqs. (3)–(5)). The yellow regions represent the ranges of hydrogen diffusivity ratios estimated from the hydrogen diffusion profiles in coexisting olivine and pyroxene of this study, while the blue regions represent the estimations from O-H absorbances in olivine and pyroxene reported in previous studies (see text for discussion). The filled circles represent the Tanzanian samples (Table 4). (For interpretation of the references to color in this figure legend, the reader is referred to the web version of this article.)

(Reid and Dawson, 1972). The cooling rates of tuff deposits can vary several orders of magnitude from ~10 to ~10^{-8} °C/s (Wallace et al., 2003); this range is consistent with the large variation of hydrogen diffusion duration recorded in these mantle xenoliths.

5. CONCLUSIONS

Based on measurements of hydrogen diffusion profiles in olivine, orthopyroxene and clinopyroxene, we suggest that hydrogen diffusivities in olivine and pyroxene are relatively similar at low temperatures (~750 to ~900 °C). By contrast, hydrogen diffusive loss observed in only olivine but not coexisting pyroxene, or complete loss of hydrogen from olivine but partial (or no) loss from pyroxene observed in all previous studies of mantle xenoliths is attributed to diffusion at high temperatures (~950 to >1200 °C). Our model reconciles the discrepancy between previous mantle xenolith studies and laboratory diffusion experiments on hydrogen diffusion in olivine and pyroxene. Furthermore, if hydrogen is not generally affected by melt-rock reaction during xenolith emplacement, pyroxene may generally preserve the hydrogen concentration of the deep mantle lithosphere.

ACKNOWLEDGEMENTS

This research is supported by NSFC grants (41590623 and 41573055). We thank Sylvie Demouchy and an anonymous reviewer for their constructive and detailed comments on an earlier version of this manuscript, and Anne Peslier for her help on diffusion modeling. We thank associate editor Chris Herd for handling our manuscript and Sylvie Demouchy and two anonymous reviewers for critical and thorough reviews of the present paper.

APPENDIX A. SUPPLEMENTARY MATERIAL

Supplementary data to this article can be found online at https://doi.org/10.1016/j.gca.2019.09.023.

REFERENCES

Aulbach S. and Rudnick R. L. (2009) Origins of non-equilibrium lithium isotopic fractionation in xenolithic peridotite minerals: Examples from Tanzania. *Chem. Geol.* **258**, 17–27.

Aulbach S., Rudnick R. L. and McDonough W. F. (2011) Evolution of the lithospheric mantle beneath the East African Rift in Tanzania and its potential signatures in rift magmas. *Geol. Soc. Am. Spec. Pap.* **478**, 105–125.

Baptiste V., Tommasi A., Vauchez A., Demouchy S. and Rudnick R. L. (2015) Deformation, hydration, and anisotropy of the lithospheric mantle in an active rift: constraints from mantle xenoliths from the North Tanzanian Divergence of the East African Rift. *Tectonophysics* **639**, 34–55.

Bell D. R. and Rossman G. R. (1992) Water in Earth's mantle: the role of nominally anhydrous minerals. *Science* **255**, 1391–1397.

Bell D. R., Ihinger P. D. and Rossman G. R. (1995) Quantitative analysis of trace OH in garnet and pyroxenes. *Am. Mineral.* **80**, 465–474.

Bell D. R., Rossman G. R., Maldener J., Endisch D. and Rauch F. (2003) Hydroxide in olivine: a quantitative determination of the absolute amount and calibration of the IR spectrum. *J. Geophys. Res.* **108**, 2105. https://doi.org/10.1029/2001JB000679.

Berghuijs J. F., Mattsson H. B. and Bosshard S. A. (2012) Eruptive and depositional characteristics of the Loolmurwak and Eledoi maar volcanoes, Lake Natron-Engaruka monogenetic volcanic field, northern Tanzania. *Geosci. Soc. New Zealand Misc. Publ.* **131A**, 106-107.

Bizimis M. and Peslier A. H. (2015) Water in Hawaiian garnet pyroxenites: implications for water heterogeneity in the mantle. *Chem. Geol.* **397**, 61–75.

Brey G. P. and Köhler T. (1990) Geothermobarometry in four-phase lherzolites II. New thermobarometers, and practical assessment of existing thermobarometers. *J. Petrol.* **31**, 1353–1378.

Bromiley G. D., Keppler H., McCammon C., Bromiley F. A. and Jacobsen S. D. (2004) Hydrogen solubility and speciation in natural, gem-quality chromian diopside. *Am. Mineral.* **89**, 941–949.

Burgi P. Y., Caillet M. and Haefeli S. (2002) Field temperature measurements at Erta'Ale Lava Lake, Ethiopia. *Bull. Volcanol.* **64**, 472–485.

Carpenter S. J. (2003) *The Kinetics of hydrogen diffusion in single-crystal orthopyroxene* Ph.D. Thesis. Pennsylvania State University.

Chen Y., Provost A., Schiano P. and Cluzel N. (2011) The rate of water loss from olivine-hosted melt inclusions. *Contrib. Mineral. Petrol.* **162**, 625–636.

Dawson J. B., Powell D. G. and Reid A. M. (1970) Ultrabasic xenoliths and lava from the Lashaine volcano, northern Tanzania. *J. Petrol.* **11**, 519–548.

Dawson J. B. and Smith J. V. (1988) Metasomatised and veined upper-mantle xenoliths from Pello Hill, Tanzania: Evidence for anomalously-light mantle beneath the Tanzanian sector of the East African Rift Valley. *Contrib. Mineral. Petrol.* **100**, 510–527.

Demouchy S. (2004) *Water in the Earth's interior: Thermodynamics and kinetics of hydrogen incorporation in olivine and wadsleyite* Ph.D. Thesis. University of Bayreuth.

Demouchy S. (2010) Diffusion of hydrogen in olivine grain boundaries and implications for the survival of water-rich zones in the Earth's mantle. *Earth Planet. Sci. Lett.* **295**, 305–313.

Demouchy S. and Mackwell S. (2003) Water diffusion in synthetic iron-free forsterite. *Phys. Chem. Miner.* **30**, 486–494.

Demouchy S. and Mackwell S. (2006) Mechanisms of hydrogen incorporation and diffusion in iron-bearing olivine. *Phys. Chem. Miner.* **33**, 347–355.

Demouchy S., Jacobsen S. D., Gaillard F. and Stern C. R. (2006) Rapid magma ascent recorded by water diffusion profiles in mantle olivine. *Geology* **34**, 429–432.

Demouchy S. and Bolfan-Casanova N. (2016) Distribution and transport of hydrogen in the lithospheric mantle: a review. *Lithos* **24**, 402–425.

Demouchy S., Thoraval C., Bolfan-Casanova N. and Manthilake G. (2016) Diffusivity of hydrogen in iron-bearing olivine at 3 GPa. *Phys. Earth Planet. Inter.* **260**, 1–13.

Demouchy S., Shcheka S., Denis C. M. M. and Thoraval C. (2017) Subsolidus hydrogen partitioning between nominally anhydrous minerals in garnet-bearing peridotite. *Am. Mineral.* **102**, 1822–1831.

Denis C. M. M., Demouchy S. and Shaw C. S. J. (2013) Evidence of dehydration in peridotites from Eifel Volcanic Field and estimates of the rate of magma ascent. *J. Volcanol. Geotherm. Res.* **258**, 85–99.

Denis C. M. M., Demouchy S. and Alard O. (2018) Heterogeneous hydrogen distribution in orthopyroxene from veined mantle peridotite (San Carlos, Arizona): Impact of melt-rock interactions. *Lithos* **302**, 298–311.

Doucet L. S., Peslier A. H., Ionov D. A., Brandon A. D., Golovin A. V., Goncharov A. G. and Ashchepkov I. V. (2014) High water contents in the Siberian cratonic mantle linked to metasomatism: an FTIR study of Udachnaya peridotite xenoliths. *Geochim. Cosmochim. Acta* **137**, 159–187.

Dyar M. D., Martin S. V., Mackwell S. J., Carpenter S., Grant C. A. and McGuire A. V. (1996) Crystal chemistry of Fe^{3+}, H^{+}, and D/H in mantle-derived augite from Dish Hill: implications for alteration during transport. *Geochem. Soc. Spec. Publ.* **5**, 289–304.

Farver J. R. (2010) Oxygen and hydrogen diffusion in minerals. *Rev. Mineral. Geochem.* **72**, 447–507.

Ferriss E., Plank T., Newcombe M., Walker D. and Hauri E. (2018) Rates of dehydration of olivines from San Carlos and Kilauea Iki. *Geochim. Cosmochim. Acta* **242**, 165–190.

Ferriss E., Plank T., Walker D. and Nettles M. (2015) The whole-block approach to measuring hydrogen diffusivity in nominally anhydrous minerals. *Am. Mineral.* **100**, 837–851.

Ferriss E., Plank T. and Walker D. (2016) Site-specific hydrogen diffusion rates during clinopyroxene dehydration. *Contrib. Mineral. Petrol.* **171**, 1–24.

Gaetani G. A., O'Leary J. A., Shimizu N., Bucholz C. E. and Newville M. (2012) Rapid reequilibration of H_2O and oxygen fugacity in olivine-hosted melt inclusions. *Geology* **40**, 915–918.

Grant K., Ingrin J., Lorand J. P. and Dumas P. (2007) Water partitioning between mantle minerals from peridotite xenoliths. *Contrib. Mineral. Petrol.* **154**, 15–34.

Guilhaumou N., Dumas P., Carr G. L. and Williams G. P. (1998) Synchrotron infrared microspectrometry applied to petrography in micrometer-scale range: fluid chemical analysis and mapping. *Appl. Spectrosc.* **52**, 1029–1034.

Hauri E. (2002) SIMS analysis of volatiles in silicate glasses, 2: isotopes and abundances in Hawaiian melt inclusions. *Chem. Geol.* **183**, 115–141.

Hauri E. H., Gaetani G. A. and Green T. H. (2006) Partitioning of water during melting of the Earth's upper mantle at H_2O-undersaturated conditions. *Earth Planet. Sci. Lett.* **248**, 715–734.

Hercule S. and Ingrin J. (1999) Hydrogen in diopside: diffusion, kinetics of extraction-incorporation, and solubility. *Am. Mineral.* **84**, 1577–1587.

Hui H., Peslier A. H., Rudnick R. L., Simonetti A. and Neal C. R. (2015) Plume-cratonic lithosphere interaction recorded by water and other trace elements in peridotite xenoliths from the Labait volcano, Tanzania. *Geochem. Geophys. Geosyst.* **16**, 1687–1710.

Ingrin J., Hercule S. and Charton T. (1995) Diffusion of hydrogen in diopside: results of dehydration experiments. *J. Geophys. Res.* **100**, 15489–15499.

Ingrin J. and Blanchard M. (2006) Diffusion of hydrogen in minerals. *Rev. Mineral. Geochem.* **62**, 291–320.

Jollands M. C., Padrón-Navarta J. A., Hermann J. and O'Neill H. S. C. (2016) Hydrogen diffusion in Ti-doped forsterite and the preservation of metastable point defects. *Am. Mineral.* **101**, 1571–1583.

Karato S. I. (2013) Theory of isotope diffusion in a material with multiple species and its implications for hydrogen-enhanced electrical conductivity in olivine. *Phys. Earth Planet. Inter.* **219**, 49–54.

Karato S. I. and Jung H. (1998) Water, partial melting and the origin of the seismic low velocity and high attenuation zone in the upper mantle. *Earth Planet. Sci. Lett.* **157**, 193–207.

Kohlstedt D. L. and Mackwell S. J. (1998) Diffusion of hydrogen and intrinsic point defects in olivine. *Z. Phys. Chem.* **207**, 147–162.

Kovács I., Green D. H., Rosenthal A., Hermann J., O'Neill H. S. C., Hibberson W. O. and Udvardi B. (2012) An experimental study of water in nominally anhydrous minerals in the upper mantle near the water-saturated solidus. *J. Petrol.* **53**, 2067–2093.

Li Z.-X. A., Lee C.-T. A., Peslier A. H., Lenardic A. and Mackwell S. J. (2008) Water contents in mantle xenoliths from the Colorado Plateau and vicinity: implications for the mantle rheology and hydration-induced thinning of continental litho-

sphere. *J. Geophys. Res.* **113**, B09210. https://doi.org/10.1029/2007JB005540.

Lloyd A. S., Plank T., Ruprecht P., Hauri E. H. and Rose W. (2013) Volatile loss from melt inclusions in pyroclasts of differing sizes. *Contrib. Mineral. Petrol.* **165**, 129–153.

Lloyd A. S., Ferriss E., Ruprecht P., Hauri E. H., Jicha B. R. and Plank T. (2016) An assessment of clinopyroxene as a recorder of magmatic water and magma ascent rate. *J. Petrol.* **57**, 1865–1886.

Luhr J. F. and Aranda-Gómez J. J. (1997) Mexican peridotite xenoliths and tectonic terranes: Correlations among vent location, texture, temperature, pressure, and oxygen fugacity. *J. Petrol.* **38**, 1075–1112.

Mackwell S. J. and Kohlstedt D. L. (1990) Diffusion of hydrogen in olivine: implications for water in the mantle. *J. Geophys. Res.* **95**, 5079–5088.

Mackwell S. J., Kohlstedt D. L. and Paterson M. S. (1985) The role of water in the deformation of olivine single crystals. *J. Geophys. Res.* **90**, 11319–11333.

Novella D., Frost D. J., Hauri E. H., Bureau H., Raepsaet C. and Roberge M. (2014) The distribution of H_2O between silicate melt and nominally anhydrous peridotite and the onset of hydrous melting in the deep upper mantle. *Earth Planet. Sci. Lett.* **400**, 1–13.

Padrón-Navarta J. A., Hermann J. and O'Neill H. S. C. (2014) Site-specific hydrogen diffusion rates in forsterite. *Earth Planet. Sci. Lett.* **392**, 100–112.

Peslier A. H., Luhr J. F. and Post J. (2002) Low water contents in pyroxenes from spinel-peridotites of the oxidized, sub-arc mantle wedge. *Earth Planet. Sci. Lett.* **201**, 69–86.

Peslier A. H. and Luhr J. F. (2006) Hydrogen loss from olivines in mantle xenoliths from Simcoe (USA) and Mexico: mafic alkalic magma ascent rates and water budget of the sub-continental lithosphere. *Earth Planet. Sci. Lett.* **242**, 302–319.

Peslier A. H., Woodland A. B. and Wolff J. A. (2008) Fast kimberlite ascent rates estimated from hydrogen diffusion profiles in xenolithic mantle olivines from southern Africa. *Geochim. Cosmochim. Acta* **72**, 2711–2722.

Peslier A. H. (2010) A review of water contents of nominally anhydrous natural minerals in the mantles of Earth, Mars, and the Moon. *J. Volcanol. Geotherm. Res.* **197**, 239–258.

Peslier A. H., Woodland A. B., Bell D. R. and Lazarov M. (2010) Olivine water contents in the continental lithosphere and the longevity of cratons. *Nature* **467**, 78–81.

Peslier A. H., Woodland A. B., Bell D. R., Lazarov M. and Lapen T. J. (2012) Metasomatic control of water contents in the Kaapvaal cratonic mantle. *Geochim. Cosmochim. Acta* **97**, 213–246.

Peslier A. H., Bizimis M. and Matney M. (2015) Water disequilibrium in olivines from Hawaiian peridotites: recent metasomatism, H diffusion and magma ascent rates. *Geochim. Cosmochim. Acta* **154**, 98–117.

Reid A. M. and Dawson J. B. (1972) Olivine-garnet reaction in peridotites from Tanzania. *Lithos* **5**, 115–124.

Rudnick R. L., Mcdonough W. F. and Orpin A. (1994) Northern Tanzanian peridotite xenoliths: a comparison with Kaapvaal peridotites and inferences on metasomatic interactions. *Proc. Int. Kimberlite Conf.* **5**, 336–353.

Satsukawa T., Godard M., Demouchy S., Michibayashi K. and Ildefonse B. (2017) Chemical interactions in the subduction factory: new insights from an in situ trace element and hydrogen study of the Ichinomegata and Oki-Dogo mantle xenoliths (Japan). *Geochim. Cosmochim. Acta* **208**, 234–267.

Shewmon P. G. (1989) *Diffusion in Solids*, second ed. The Minerals, Metals & Materials Society, Warrendale, PA.

Skogby H. and Rossman G. R. (1989) OH^- in pyroxene: an experimental study of incorporation mechanisms and stability. *Am. Mineral.* **74**, 1059–1069.

Stalder R. and Skogby H. (2003) Hydrogen diffusion in natural and synthetic orthopyroxene. *Phys. Chem. Miner.* **30**, 12–19.

Stalder R. and Skogby H. (2007) Dehydration mechanisms in synthetic Fe-bearing enstatite. *Eur. J. Mineral.* **19**, 201–216.

Stalder R. and Behrens H. (2006) D/H exchange in pure and Cr-doped enstatite: implications for hydrogen diffusivity. *Phys. Chem. Miner.* **33**, 601–611.

Stalder R., Purwin H. and Skogby H. (2007) Influence of Fe on hydrogen diffusivity in orthopyroxene. *Eur. J. Mineral.* **19**, 899–903.

Stalder R., Klemme S., Ludwig T. and Skogby H. (2005) Hydrogen incorporation in orthopyroxene: interaction of different trivalent cations. *Contrib. Mineral. Petrol.* **150**, 473–485.

Sundvall R., Skogby H. and Stalder R. (2009a) Dehydration-hydration mechanisms in synthetic Fe-poor diopside. *Eur. J. Mineral.* **21**, 17–26.

Sundvall R., Skogby H. and Stalder R. (2009b) Hydrogen diffusion in synthetic Fe-free diopside. *Eur. J. Mineral.* **21**, 963–970.

Sundvall R. and Skogby H. (2011) Hydrogen defect saturation in natural pyroxene. *Phys. Chem. Miner.* **38**, 335–344.

Sundvall R. and Stalder R. (2011) Water in upper mantle pyroxene megacrysts and xenocrysts: a survey study. *Am. Mineral.* **96**, 1215–1227.

Tenner T. J., Hirschmann M. M., Withers A. C. and Hervig R. L. (2009) Hydrogen partitioning between nominally anhydrous upper mantle minerals and melt between 3 and 5 GPa and applications to hydrous peridotite partial melting. *Chem. Geol.* **262**, 42–56.

Thoraval C. and Demouchy S. (2014) Numerical models of ionic diffusion in one and three dimensions: application to dehydration of mantle olivine. *Phys. Chem. Miner.* **41**, 709–723.

Tian Z. Z., Liu J., Xia Q.-K., Ingrin J., Hao Y. T. and Christophe D. (2017) Water concentration profiles in natural mantle orthopyroxenes: a geochronometer for long annealing of xenoliths within magma. *Geology* **45**, 87–90.

Tollan P. M. E., O'Neill H. S. C., Hermann J., Benedictus A. and Arculus R. J. (2015) Frozen melt–rock reaction in a peridotite xenolith from sub-arc mantle recorded by diffusion of trace elements and water in olivine. *Earth Planet. Sci. Lett.* **422**, 169–181.

Wallace P. J., Dufek J., Anderson A. T. and Zhang Y. (2003) Cooling rates of Plinian-fall and pyroclastic-flow deposits in the Bishop Tuff: inferences from water speciation in quartz-hosted glass inclusions. *Bull. Volcanol.* **65**, 105–123.

Wang D., Mookherjee M., Xu Y. and Karato S. (2006) The effect of water on the electrical conductivity of olivine. *Nature* **443**, 977–980.

Warren J. M. and Hauri E. H. (2014) Pyroxenes as tracers of mantle water variations. *J. Geophys. Res.* **119**, 1851–1881.

Weis F. A., Stalder R. and Skogby H. (2016) Experimental hydration of natural volcanic clinopyroxene phenocrysts under hydrothermal pressures (0.5–3 kbar). *Am. Mineral.* **101**, 2233–2247.

Withers A. C., Bureau H., Raepsaet C. and Hirschmann M. M. (2012) Calibration of infrared spectroscopy by elastic recoil detection analysis of H in synthetic olivine. *Chem. Geol.* **334**, 92–98.

Woods S. C., Mackwell S. and Dyar D. (2000) Hydrogen in diopside: Diffusion profiles. *Am. Mineral.* **85**, 480–487.

Xia Q., Chen D., Carpenter S., Zhi X., Wang R. and Cheng H. (2000) Hydrogen diffusion in clinopyroxene: dehydration experiments. *Sci. China Ser. D Earth Sci.* **43**, 561–568.

Xia Q.-K., Hao Y., Li P., Deloule E., Coltorti M., Dallai L., Yang X. and Feng M. (2010) Low water content of the Cenozoic lithospheric mantle beneath the eastern part of the North China Craton. *J. Geophys. Res.* **115**, B07207. https://doi.org/10.1029/2009JB006694.

Yu Y., Xu X.-S., Griffin W. L., O'Reilly S. Y. and Xia Q.-K. (2011) H_2O contents and their modification in the Cenozoic subcontinental lithospheric mantle beneath the Cathaysia block, SE China. *Lithos* **126**, 182–197.

Associate Editor: Christopher Herd